



Enhancement and Speed-Up of Carrier Dynamics in A Dielectric Nanocavity with Deep Sub-Wavelength Confinement

Dong, Gaoneng; Babar, Ali Nawaz; Christiansen, Rasmus Ellebæk; Hansen, Søren Engelberth; Stobbe, Søren; Yu, Yi; Mørk, Jesper

Published in:
Laser and Photonics Reviews

Link to article, DOI:
[10.1002/lpor.202500895](https://doi.org/10.1002/lpor.202500895)

Publication date:
2026

Document Version
Publisher's PDF, also known as Version of record

[Link back to DTU Orbit](#)

Citation (APA):
Dong, G., Babar, A. N., Christiansen, R. E., Hansen, S. E., Stobbe, S., Yu, Y., & Mørk, J. (in press). Enhancement and Speed-Up of Carrier Dynamics in A Dielectric Nanocavity with Deep Sub-Wavelength Confinement. *Laser and Photonics Reviews*. <https://doi.org/10.1002/lpor.202500895>

General rights

Copyright and moral rights for the publications made accessible in the public portal are retained by the authors and/or other copyright owners and it is a condition of accessing publications that users recognise and abide by the legal requirements associated with these rights.

- Users may download and print one copy of any publication from the public portal for the purpose of private study or research.
- You may not further distribute the material or use it for any profit-making activity or commercial gain
- You may freely distribute the URL identifying the publication in the public portal

If you believe that this document breaches copyright please contact us providing details, and we will remove access to the work immediately and investigate your claim.

RESEARCH ARTICLE OPEN ACCESS

Enhancement and Speed-Up of Carrier Dynamics in A Dielectric Nanocavity with Deep Sub-Wavelength Confinement

Gaoneng Dong^{1,2}  | Ali Nawaz Babar^{1,2} | Rasmus Ellebæk Christiansen^{2,3} | Søren Engelberth Hansen^{1,2} | Søren Stobbe^{1,2} | Yi Yu^{1,2} | Jesper Mørk^{1,2}

¹Department of Electrical and Photonics Engineering, Technical University of Denmark, Kongens Lyngby, Denmark | ²NanoPhoton - Center for Nanophotonics, Technical University of Denmark, Kongens Lyngby, Denmark | ³Department of Civil and Mechanical Engineering, Technical University of Denmark, Kongens Lyngby, Denmark

Correspondence: Søren Stobbe (ssto@dtu.dk) | Yi Yu (yiyu@dtu.dk) | Jesper Mørk (jesm@dtu.dk)

Received: 15 April 2025 | **Revised:** 7 October 2025 | **Accepted:** 19 October 2025

Keywords: all-optical switching | deep sub-wavelength confinement | dielectric nanocavity | light-matter interactions | ultrafast dynamics

ABSTRACT

Dielectric bowtie cavities represent a breakthrough in simultaneously achieving ultrahigh quality factors and ultra-small mode volumes, providing new opportunities for enhancing light-matter interactions. Experimental work has so far emphasized the realization of these nanocavities. Here, we experimentally investigate the ultrafast dynamics of a topology-optimized dielectric (silicon) bowtie nanocavity, with device dimensions down to 12 nm, that localizes light to a mode volume deep below the so-called diffraction limit given by the half-wavelength cubed. This strong spatial light concentration is shown to significantly enhance the carrier generation rate through two-photon absorption, as well as reducing the time it takes for the carriers to recover. A diffusion time below 1 ps is achieved for the bowtie cavity, which is more than an order of magnitude smaller than for a conventional nanocavity. Additionally, parametric effects due to coherent interactions between pump and probe signals are also enhanced in the bowtie cavity, leading to an improved extinction ratio. These results demonstrate important fundamental advantages of dielectric bowtie cavities compared to conventional point-defect cavities, laying a foundation for novel low-power and ultrafast optical devices, including switches and modulators.

1 | Introduction

Optical microcavities [1] can significantly enhance the interaction between light and matter by providing strong spatial and spectral confinement, which is important for many applications, such as nanolasers [2–8], nonlinear photonics [9–14], sensing [15], cavity quantum electrodynamics [16–19], and optomechanics [20–22]. Traditional dielectric cavities, such as photonic crystal cavities, provide strong spectral confinement, while the spatial localization for such dielectric cavities for a long time was considered to be limited to mode volumes, V_p , larger than the so-called diffraction

limit, $V_\lambda = (\lambda/(2n))^3$, with λ and n being the vacuum wavelength and the material refractive index, respectively. Plasmonic cavities [23–25], on the other hand, are well-known to confine light deep below the wavelength, albeit at the cost of ohmic losses, which limit the spectral confinement [26]. Recently, however, a new class of dielectric nanocavities has emerged, so-called bowtie cavities [27–32], with experimentally demonstrated mode volumes down to $V_p = 0.08V_\lambda$ [33]. Such extreme dielectric confinement (EDC) can be explained by the slot-antislotted effect [31, 34], driven by the boundary conditions of the electromagnetic field, whereby the energy density of the electromagnetic field can be enhanced in

This is an open access article under the terms of the [Creative Commons Attribution-NonCommercial-NoDeriv](https://creativecommons.org/licenses/by-nc-nd/4.0/) License, which permits use and distribution in any medium, provided the original work is properly cited, the use is non-commercial and no modifications or adaptations are made.

© 2025 The Author(s). *Laser & Photonics Reviews* published by Wiley-VCH GmbH

a structure with bowtie geometry. Although there are a few works that explored strong spatial light confinement, they focused on structures where the optical field is maximized in air [27], rather than in dielectrics. While the primary motivation for realizing such EDC cavities is to enhance light–matter interaction, their influence on carrier dynamics has not yet been experimentally investigated.

In this work, we experimentally study the dynamics of a bowtie cavity with deep sub-wavelength confinement of light. The cavity is designed using fabrication-constrained topology optimization while maintaining efficient waveguide-cavity coupling. The fabricated devices are characterized using a heterodyne pump-probe technique and show that, compared to a reference cavity with conventional confinement, the bowtie cavity not only enhances the strength of optical switching but also reduces the recovery time. We analyze the bowtie cavities using temporal coupled-mode theory and simulations of spatio-temporal carrier dynamics. The comparison with experimental data shows that both incoherent processes due to enhanced two-photon absorption (TPA) as well as parametric interactions due to four-wave mixing between pump and probe are enhanced in the bowtie cavity. A diffusion time below 1 ps is achieved for the bowtie cavity, which is more than an order of magnitude smaller than for a conventional nanocavity. Since the light-matter interaction is enhanced using a small optical mode volume rather than a high quality factor, the bandwidth of the device is not compromised, thus facilitating the development of high-speed applications, such as all-optical switching [10, 12] and modulators [35–37].

2 | Structure and Switching Dynamics

The bowtie cavity, designed using topology optimization [38] employing appropriate fabrication constraints [39] (see Section S1), is realized in a nanobeam geometry. It features an electromagnetic field profile with a strongly localized hotspot in the region between the two tips of the bowtie, as illustrated in Figure 1a. The nanobeam bowtie cavity distinguishes itself from previous 2D structures [33, 40] with two major benefits. First, it seamlessly integrates input and output waveguides, which can be co-optimized with the cavity. The waveguide integration results in a power transmission coefficient of 91% (−0.41 dB) at the resonant frequency. In contrast to other nanobeam implementations [41], the design features a single rather than multiple hotspots, making it better suited for switching applications. Second, the nanobeam has a footprint of just 3.0 μm^2 , which is 20%–30% of that occupied by previous 2D bowtie cavities [33, 40]. We note that the bowtie cavity was intentionally designed with a modest quality factor of about 1000, consistent with the short pulses used in the experiment. Much higher quality factors—relevant, for example, to laser applications—can be achieved through design optimization; however, this typically entails a trade-off between mode volume and quality factor [42].

To enable a one-to-one comparison of the dynamics of the bowtie cavity to conventional point-defect cavities, we also designed a reference nanobeam cavity in the same material platform (Figure 1b). The reference cavity has characteristics comparable to conventional nanobeam cavities [43], including the electric field distribution, quality factor, and mode volumes,

while maintaining a similar footprint (see Section S2). These similarities extend to the carrier dynamics, which is close to that of conventional nanobeam cavities. It is emphasized that the fabrication uncertainties were incorporated into the topology optimization for both cavities, resulting in fabricated geometries (Figure 1c,d) that closely mirror the designed structures (Figure 1a,b).

The temporal dynamics of the devices were measured using a short-pulse pump-probe technique that allows co-polarized pump and probe pulses by using heterodyne detection [44] (see Section S4). The measured total quality factor and peak transmission of the characterized bowtie (reference) cavity are 700 (1200) and −0.82 dB (−0.47 dB), respectively, corresponding to an intrinsic quality factor of 7800 (23 000) (see Section S5). Representative dynamic measurements are shown in Figure 1e,f for the bowtie cavity and the reference cavity, respectively, considering both cases of red and blue detuning of the probe with respect to the pump (aligned to the cold cavity resonance). For the bowtie cavity, we observe a fast decrease (increase) in the transmittance of the red-detuned (blue-detuned) probe light after the arrival of an intense pump pulse with a pulse width of 0.93 ps. After the pump pulse, the probe transmittance recovers almost entirely within 2 ps. The amplitude of the slowly varying tail amounts to only one-tenth of the total change, and the extinction ratio is −5.7 dB for the red-detuned probe wavelength. In contrast, the pump-probe signal for the reference cavity shows an extinction ratio of −2.3 dB at the same injected pump energy, and has more pronounced slow tails (Figure 1f).

In order to interpret the data, we model the probe transmission dynamics using coupled-mode theory, accounting for the generation of free carriers in the cavity region by TPA, as well as coherent wave mixing between the pump and probe pulses due to oscillations of the carrier density mediated by beating [45, 46] (see Section S3). The simulated results, solid blue curves in Figure 1e,f, agree well with measurements when using the parameter values given in Table S3 of the supplement. If parametric processes are neglected in the model, represented by the dashed red curves, the experimental data cannot be fitted by the theory in a time interval around zero delay, where the pump and probe pulses temporally overlap. On the other hand, the slower components are still well represented by the model.

Based on these results, a simple physical picture emerges for the dynamics induced by the pump, cf. Figure 2. The main effect is the generation of free carriers by TPA of the pump pulse. Due to free-carrier dispersion and band-filling, these carriers change the refractive index in the region where they are generated, i.e., in the nanocavity. This leads to an incoherent and a coherent (parametric) change of the probe transmission, cf. Figure 2b.

The incoherent effect is the shift of the resonance frequency of the cavity, cf. Figure 2b i), which changes the transmission of the probe field. Since the cavity resonance always blue shifts with increased carrier density, the sign of the probe amplitude change depends on the position of the probe wavelength relative to the cavity resonance. The relaxation time of the probe amplitude change is instead determined by the temporal variation of the spatial overlap between the carrier distribution and the probe mode profile.

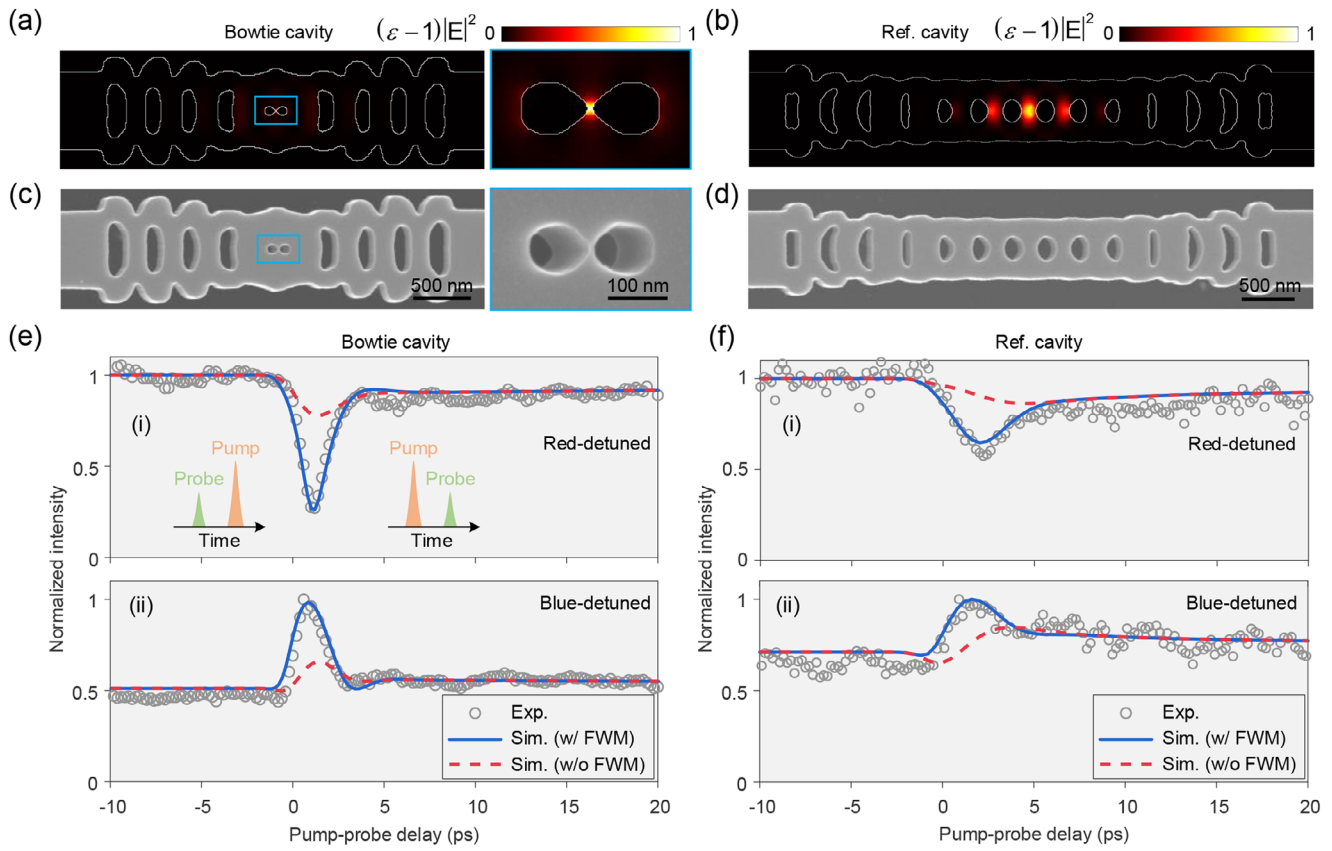


FIGURE 1 | Ultrafast dynamics of a nanobeam bowtie cavity. a,b) Normalized electric field intensity of the mode of the nanobeam bowtie cavity (a) and reference (Ref.) cavity (b) in the central plane. The inset on the right of (a) is an enlarged view of the central bowtie region. c,d) SEM images of the nanobeam bowtie cavity (c) and reference cavity (d). e,f) Representative (normalized) probe transmission dynamics as a function of the pump-probe delay for a red-detuned (i) and blue-detuned (ii) probe wavelength in the e) nanobeam bowtie cavity and f) reference cavity. In (e) and (f), the gray circle marks are the experimental (Exp.) results, while the solid blue and dashed red curves represent the simulations (Sim.) with (w/) and without (w/o) four-wave mixing (FWM), respectively. The pump pulse energy coupled into the waveguide is 255 fJ in (e) and (f).

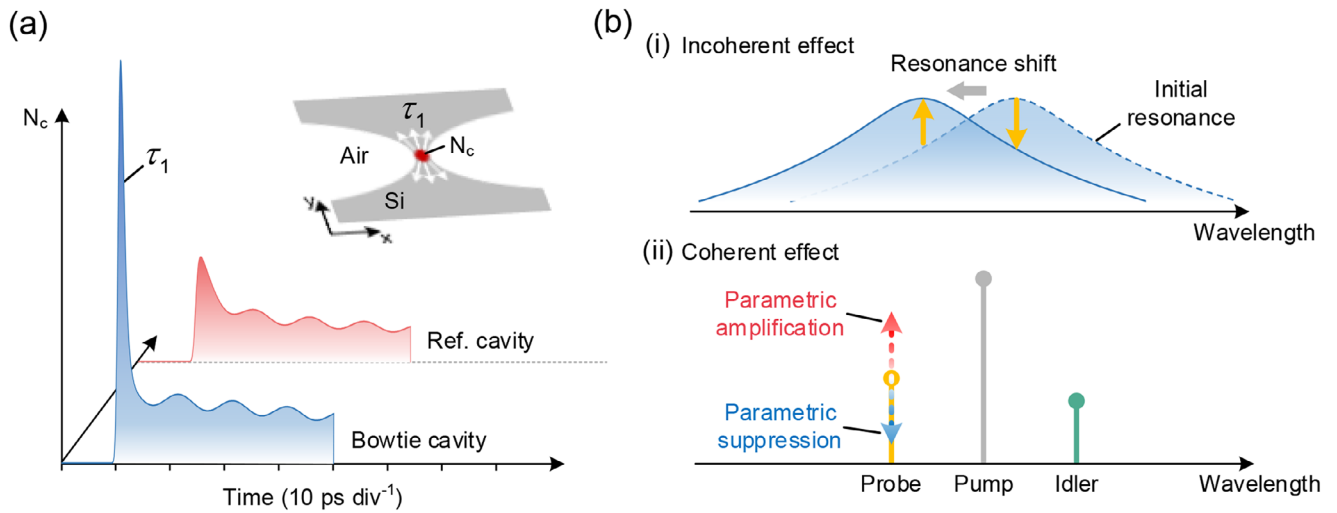


FIGURE 2 | Physical mechanisms. (a) Time evolution (calculated with the parameters given in Table S3 of the supplement, but using the same quality factor ($Q_t = 700$) and pump pulse width (0.93 ps) for both cavities) of the mode-averaged carrier density, N_c , in the bowtie cavity (blue shaded area) and reference cavity (red shaded area). The inset illustrates the carrier diffusion process in the central plane of the cavity mode region of the bowtie cavity. (b) Working principle in the frequency domain. (i) Incoherent effect: probe transmission change caused by the frequency shift of the cavity resonance. (ii) Coherent effect: probe transmission change induced by the parametric amplification or suppression process.

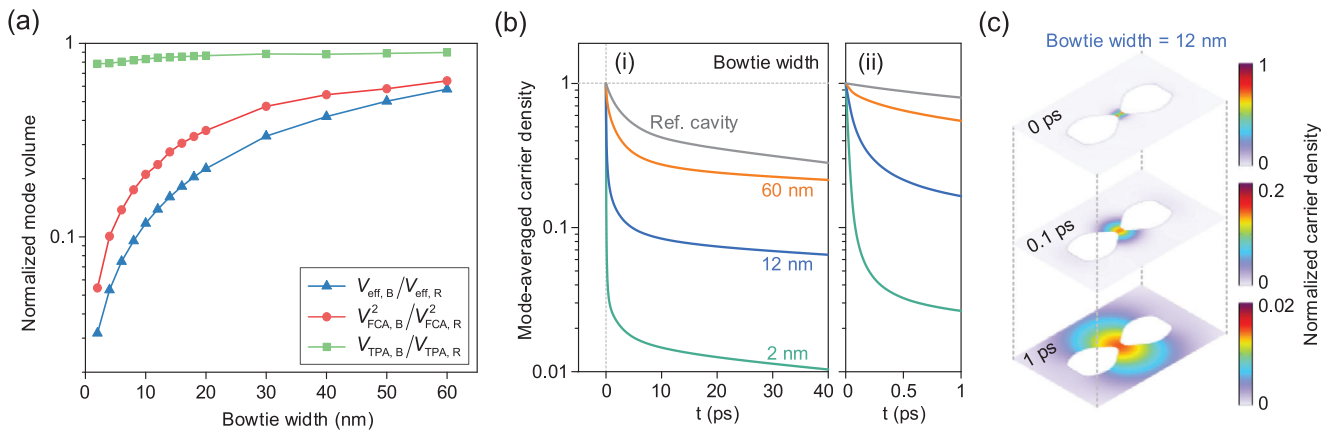


FIGURE 3 | Mode volumes and carrier diffusion. (a) Calculated effective mode volume, V_{eff} , square of free-carrier absorption (FCA) mode volume, V_{FCA} , and two-photon absorption (TPA) mode volume, V_{TPA} , of the nanobeam bowtie cavity (B) vs width of the bowtie bridge. These mode volumes are normalized by corresponding mode volumes of the reference cavity (R). (b) Calculated (normalized) carrier relaxation process for the nanobeam bowtie cavity with different bowtie widths (2, 12, and 60 nm) and the reference cavity. (ii) shows a zoom-in on the short-time-scale dynamics in (i). (c) Calculated free carrier distribution in the central plane of the bowtie region (bowtie width = 12 nm) at different times (0, 0.1, and 1 ps). The carrier distributions are normalized by the maximum carrier density at 0 ps.

The parametric effect is caused by the temporal oscillation of the free carrier density, cf. Figure 2a, due to beating between the co-polarized pump and probe fields. This establishes a temporal grating that scatters photons between the pump and probe wavelengths, accompanied by the generation of an idler signal, cf. Figure 2b ii). Whether the probe field is amplified or attenuated depends on the phase-matching condition between the pump light, the probe light, and the oscillating carrier density [46]. Since the pump and probe fields only beat when the pulses overlap, this effect is limited to a time window around zero pump-probe delay.

The resulting probe dynamics is the combination of these effects. Both the larger amplitude variation and the shorter time scale of the dynamics seen in the bowtie cavity (Figure 1e) compared to the reference cavity (Figure 1f) originate from the stronger spatial localization of light in the bowtie region. The localization enhances the carrier generation rate since this happens via a nonlinear process (TPA in our case), and the time scale for re-equilibration after the pump pulse shortens due to the larger spatial gradient of the carrier distribution, which enhances the diffusion process. Next, we quantify these effects through an analysis of the characteristic mode volumes.

3 | Mode Volumes and Carrier Diffusion

The strengths of linear and nonlinear optical processes in a cavity scale with different mode volumes [47, 48]. To quantify these, we calculate the effective (linear) mode volume, V_{eff} , as well as the nonlinear mode volumes, i.e., the free-carrier absorption (FCA) mode volume, V_{FCA} , and the TPA mode volume, V_{TPA} [33, 47, 48] (see Section S2), as shown in Figure 3a.

It is important to recognize that the carrier generation rate, G_N , due to TPA scales inversely with the square of the FCA mode volume, i.e., $G_N \propto 1/V_{\text{FCA}}^2$ [10]. Conversely, the TPA loss, γ_{TPA} , is inversely proportional to the TPA mode volume, i.e., $\gamma_{\text{TPA}} \propto 1/V_{\text{TPA}}$ (see Section S3). Across a wide range (2–60 nm)

of bowtie widths, the FCA mode volume is significantly smaller than that of the reference cavity. Notably, as the width of the bowtie bridge narrows, there is a pronounced reduction in the FCA mode volume. Consequently, when subjected to identical pump pulse energies, the carrier generation rate is significantly higher in the bowtie cavity than in the reference cavity, as illustrated in Figure 2a. This leads to a larger resonance shift (will be further illustrated in Figure 4), as well as a larger probe transmission change induced by the parametric processes (Figure 1e). Remarkably, while the FCA mode volume of the bowtie cavity diminishes rapidly with the bowtie width, the TPA mode volume exhibits only a minor reduction and is on par with that of the reference cavity. This suggests that the bowtie cavity imparts a larger dynamical change of the transmission without a corresponding increase in TPA loss. Although the FCA loss in the bowtie cavity is also increased due to the smaller V_{FCA} , this only results in a small decrease in the extinction ratio according to our calculations (see Section S7). The qualitatively different dependencies of the various mode volume measures on the bowtie bridge width are noteworthy, as they may point to distinct spatial characteristics of the nonlinear interactions. However, it is, to the best of our knowledge, not yet clear whether this behavior is a generic feature of all similar designs.

The effective mode volume does not directly impact the amplitude of the dynamical change of the probe, but is important for the speed of the carrier diffusion process, as previously demonstrated in photonic crystal nanocavities [12, 49]. The cavity with a smaller effective mode volume results in a faster carrier relaxation process due to the larger spatial gradients of free carriers in the cavity mode region.

Figure 3b shows the calculated carrier relaxation processes for the bowtie cavity with different bowtie widths and the reference cavity using the ambipolar-diffusion model [49, 50]. The results show that the carriers in the bowtie cavity diffuse out of the cavity mode region much faster than the reference cavity over a wide range of bowtie widths. This advantage of the bowtie

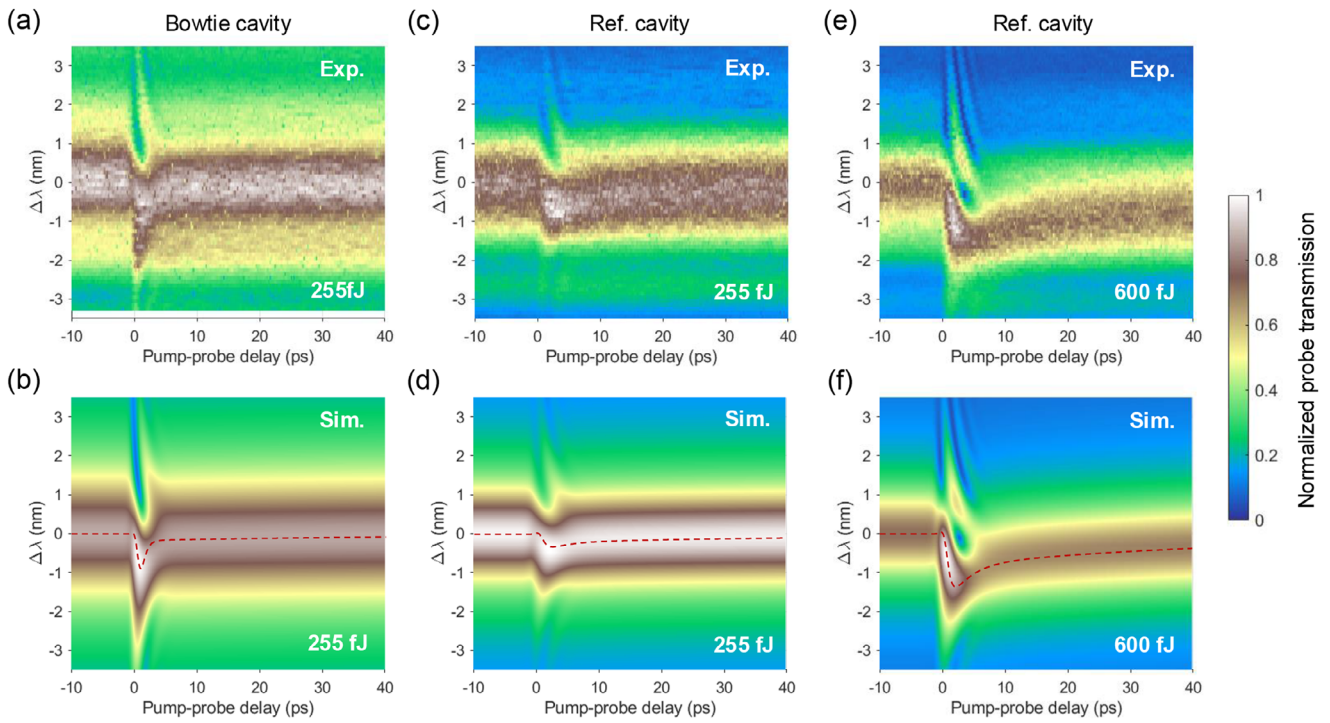


FIGURE 4 | Wavelength-dependent dynamics. (a), (b) Measured (a) and calculated (b) probe transmission dynamics of the nanobeam bowtie cavity for a pump pulse energy of 255 fJ. (c), (d) Measured (c) and calculated (d) probe transmission dynamics of the reference cavity for a pump pulse energy of 255 fJ. (e), (f) Measured (e) and calculated (f) probe transmission dynamics of the reference cavity for a pump pulse energy of 600 fJ. The red dashed curves in (b), (d), and (f) represent the corresponding cavity resonance shifts.

cavity becomes more significant as the bowtie width decreases. Representative time-dependent carrier distributions of the bowtie cavity (bowtie width = 12 nm) show that the maximum carrier density decreases by more than 50 times within 1 ps (Figure 3c).

The carrier relaxation process consists of a fast and a slow component (Figure 3b). According to our calculations (see Section S2), both the fast and slow components are mainly determined by carrier diffusion when the surface recombination rate is lower than 10^5 cm/s. For the experimentally characterized bowtie cavity with a bowtie width of 12 nm, the calculated fast diffusion time is approximately 0.3 ps, while this value drops to tens of fs when the bowtie width is reduced to 2 nm. In contrast, the fast diffusion time of the reference cavity is 6 ps, which is more than one order of magnitude larger than that of the bowtie cavity. It is noteworthy that the bowtie cavity not only has a shorter fast diffusion time than the reference cavity, but also has a larger relative amplitude of the fast diffusion component. This is why the slow recovery component, reflecting slow diffusion and non-radiative recombination, is strongly suppressed in the bowtie cavity (Figure 1e) compared to the reference cavity (Figure 1f).

4 | Wavelength-Dependent Dynamics

To further investigate the dynamics, in particular the differences between the bowtie and the reference cavity, we compared experimental and theoretical results for the wavelength and time-dependent variation of the probe signal, cf. Figure 4. Figure 4a,b show results for the bowtie cavity for a fixed pump wavelength coinciding with the cold cavity resonance and an injected pump

pulse energy of 255 fJ at the input waveguide. Good agreement between experiment and theory is obtained using the set of parameters given in Table S3 of the supplement. The red dashed curve represents the resonance shift of the bowtie cavity, indicating a switching window of 1.5 ps as evaluated from the full width at half the maximum resonance shift. The fast diffusion time used for the fitting is 0.6 ps, which is comparable to the numerically simulated result of 0.3 ps obtained using the ambipolar-diffusion model. This slight discrepancy is attributed to differences in initial carrier distributions: the numerical simulation assumes an idealized spatial profile proportional to the square of the cavity field intensity ($|E|^4$), while the experimental result inherently includes the effects of finite pump pulse width and cavity photon lifetime, both of which are on the same timescale as the fast diffusion process. The simulated probe transmission dynamics in the absence of the parametric process are also shown (see Section S3), indicating that the ultrafast probe transmission increase (decrease) is dominated by the parametric process while the slow recovery tail depends on the cavity resonance shift. The significance of the parametric process in a time-window around zero pump-probe delay was confirmed experimentally by using the heterodyne technique to measure the idler signal [46]. As shown in Section S6, the idler signal only exists in the time-window around zero pump-probe delay, confirming the coherent nature of this process.

Results for the reference cavity (Figure 4c,d), also conducted with the pump pulse in resonance with the cavity and for the same pump pulse energy of 255 fJ, show that the probe change due to both the parametric process (ripples around zero pump-probe delay) and the cavity resonance shift (represented by the

red dashed curves) are significantly weaker than for the bowtie cavity, despite the quality factor of the reference cavity being significantly higher. Although the resonance shift is relatively small for the reference cavity, the slow recovery process is clearly visible (Figure 4c,d). The slow-down of the diffusion process is even more apparent if the experiment is carried out for a higher pump pulse energy (Figure 4e,f). The features seen in Figure 4c–f for the reference cavity are very similar to those observed in a photonic crystal H0 cavity [45], but differ significantly from the bowtie cavity. The estimated switching window for the bowtie cavity (1.5 ps) is approximately an order of magnitude smaller than the 18-ps switching window observed in the reference cavity.

5 | Discussion and Conclusion

Although the pump power required to achieve a given resonance shift is already lower for the bowtie cavity with a bridge width of 12 nm than for the reference cavity, the pump power can be further reduced by reducing the bowtie width due to the scaling with the nonlinear mode volume, V_{FCA} . It should be noted, though, that when the bowtie width decreases, the faster diffusion of free carriers counteracts the accumulation of carriers in the modal region, thereby limiting the reduction of the energy consumption. However, on the positive side, the fast diffusion reduces the amplitude of the slow tail. A bowtie cavity with a smaller bowtie width may be achieved through thickness-controlled surface oxidation and subsequent oxide layer removal [51, 52]. The pump power can also be significantly reduced by using other materials, such as InP [10] and GaAs [13], whose TPA coefficients are more than one order of magnitude larger than Si. Finally, we also evaluated the impact of sidewall slope on the performance of the bowtie cavity. Simulations with slant angles ranging from 0° to 4°, reflecting realistic fabrication tolerances, indicate a ~10% reduction in quality factor, a ~3 nm redshift in resonance, and a ~27% increase in effective mode volume for a nominal bowtie width of 12 nm. These results suggest that the bowtie cavity design remains robust even in the presence of moderate sidewall angle variations.

In summary, we experimentally investigate the ultrafast dynamics of a dielectric cavity featuring a bowtie nanostructure that enables sub-wavelength confinement of light inside the semiconductor material. Both theoretical and experimental results show that the bowtie cavity significantly improves the all-optical switching dynamics, owing to an ultra-small linear mode volume as well as an ultra-small nonlinear mode volume. The smaller linear mode volume significantly speeds up the carrier diffusion process and strongly suppresses the slow recovery tail commonly associated with switches. The smaller nonlinear mode volume improves the switching contrast through both coherent and incoherent effects. These results establish the dielectric bowtie cavity as a new and strong candidate for low-power and ultrafast optical devices, including switches [9, 10, 12] and modulators [35–37].

Acknowledgements

G.D. and A.B. contributed equally to this work. The authors gratefully acknowledge funding by Danish National Research Foundation (Grant

No. DNR147 NanoPhoton), the European Research Council (ERC) under the European Union Horizon 2020, Research and Innovation Programme (Grant Nos. 834410 FANO and 101045396 SPOTLIGHT), the Villum Fonden via the Young Investigator Program (Grant No. 42026 EXTREME), and the Innovation Fund Denmark (Grant No. 0175-00022—NEXUS).

Conflicts of Interest

The authors declare no conflicts of interest.

Data Availability Statement

The data that support the findings of this study are available from the corresponding author upon reasonable request.

References

1. K. J. Vahala, "Optical Microcavities," *Nature* 424 (2003): 839–846, <https://doi.org/10.1038/nature01939>.
2. M. T. Hill and M. C. Gather, "Advances in Small Lasers," *Nature Photonics* 8 (2014): 908–918, <https://doi.org/10.1038/nphoton.2014.239>.
3. E. Dimopoulos, M. Xiong, and A. Sakanas, "Experimental Demonstration of a Nanolaser with a Sub- μ A Threshold Current," *Optica* 10 (2023): 973, <https://doi.org/10.1364/OPTICA.488604>.
4. G. Crosnier, D. Sanchez, and S. Bouchoule, "Hybrid Indium Phosphide-on-Silicon Nanolaser Diode," *Nature Photonics* 11 (2017): 297–300, <https://doi.org/10.1038/nphoton.2017.56>.
5. K. Takeda, T. Sato, and A. Shinya, "Few-fJ/Bit Data Transmissions Using Directly Modulated Lambda-Scale Embedded Active Region Photonic-Crystal Lasers," *Nature Photonics* 7 (2013): 569–575, <https://doi.org/10.1038/nphoton.2013.110>.
6. K.-Y. Jeong, Y.-S. No, and Y. Hwang, "Electrically Driven Nanobeam Laser," *Nature Communications* 4 (2013): 2822, <https://doi.org/10.1038/ncomms3822>.
7. B. Ellis, M. A. Mayer, and G. Shambat, "Ultralow-threshold Electrically Pumped Quantum-Dot Photonic-Crystal Nanocavity Laser," *Nature Photonics* 5 (2011): 297–300, <https://doi.org/10.1038/nphoton.2011.51>.
8. H.-G. Park, S.-H. Kim, and S.-H. Kwon, "Electrically Driven Single-Cell Photonic Crystal Laser," *Science* 305 (2004): 1444, <https://doi.org/10.1126/science.1100968>.
9. G. Moille, S. Combrié, and L. Morgenroth, "Integrated All-Optical Switch with 10 ps Time Resolution Enabled by ALD," *Laser & Photonics Reviews* 10 (2016): 409–419, <https://doi.org/10.1002/lpor.201500197>.
10. Y. Yu, E. Palushani, and M. Heuck, "Switching Characteristics of an InP Photonic Crystal Nanocavity: Experiment and Theory," *Optics Express* 21 (2013): 31047–31061, <https://doi.org/10.1364/OE.21.031047>.
11. K. Nozaki, A. Shinya, and S. Matsuo, "Ultralow-Power All-Optical RAM Based on Nanocavities," *Nature Photonics* 6 (2012): 248–252, <https://doi.org/10.1038/nphoton.2012.2>.
12. K. Nozaki, T. Tanabe, and A. Shinya, "Sub-Femtojoule All-Optical Switching Using a Photonic-Crystal Nanocavity," *Nature Photonics* 4 (2010): 477–483, <https://doi.org/10.1038/nphoton.2010.89>.
13. C. Husko, A. De Rossi, S. Combrié, Q. V. Tran, F. Raineri, and C. W. Wong, "Ultrafast All-optical Modulation in GaAs Photonic Crystal Cavities," *Applied Physics Letters* 94 (2009): 021111, <https://doi.org/10.1063/1.3068755>.
14. T. Tanabe, M. Notomi, S. Mitsugi, A. Shinya, and E. Kuramochi, "All-Optical Switches on a Silicon Chip Realized Using Photonic Crystal Nanocavities," *Applied Physics Letters* 87 (2005): 151112.
15. G. Shambat, S.-R. Kothapalli, and J. Provine, "Single-cell Photonic Nanocavity Probes," *Nano Letters* 13 (2013): 4999–5005, <https://doi.org/10.1021/nl304602d>.

16. A. Sipahigil, R. E. Evans, D. D. Sukachev, et al., "An Integrated Diamond Nanophotonics Platform for Quantum-Optical Networks," *Science* 354 (2016): 847–850.
17. P. Lodahl, S. Mahmoodian, and S. Stobbe, "Interfacing Single Photons and Single Quantum Dots with Photonic Nanostructures," *Reviews of Modern Physics* 87 (2015): 347–400.
18. T. G. Tiecke, J. D. Thompson, N. P. de Leon, et al., "Nanophotonic Quantum Phase Switch with a Single Atom," *Nature* 508 (2014): 241–244.
19. S. Noda, M. Fujita, and T. Asano, "Spontaneous-Emission Control by Photonic Crystals and Nanocavities," *Nature Photonics* 1 (2007): 449–458.
20. J. D. Cohen, S. M. Meenehan, G. S. MacCabe, et al., "Phonon Counting and Intensity Interferometry of a Nanomechanical Resonator," *Nature* 520 (2015): 522–525.
21. A. H. Safavi-Naeini, T. P. Mayer Alegre, J. Chan, et al., "Electromagnetically Induced Transparency and Slow Light with Optomechanics," *Nature* 472 (2011): 69–73.
22. M. Eichenfield, R. Camacho, J. Chan, K. J. Vahala, and O. Painter, "A Picogram- and Nanometre-scale Photonic-crystal Optomechanical Cavity," *Nature* 459 (2009): 550–555.
23. J. Xu, T. Zhang, Y. Li, et al., "Room-temperature Low-threshold Plasmonic Nanolaser Through Mode-tailoring at Communication Wavelengths," *Laser & Photonics Reviews* 17 (2022): 2200322.
24. M. Khajavikhan, A. Simic, M. Katz, et al., "Thresholdless Nanoscale Coaxial Lasers," *Nature* 482 (2012): 204–207.
25. R. F. Oulton, V. J. Sorger, T. Zentgraf, et al., "Plasmon Lasers at Deep Subwavelength Scale," *Nature* 461 (2009): 629–632.
26. M. S. Hwang, J. H. Choi, K. Y. Jeong, et al., "Recent Advances in Nanocavities and Their Applications," *Chemical Communications (Cambridge, England)* 57 (2021): 4875–4885.
27. Y. H. Ouyang, H. Y. Luan, Z. W. Zhao, W. Z. Mao, and R. M. Ma, "Singular Dielectric Nanolaser With Atomic-scale Field Localization," *Nature* 632 (2024): 287–293.
28. A. N. Babar, T. A. S. Weis, and K. Tsoukalas, "Self-assembled Photonic Cavities With Atomic-scale Confinement," *Nature* 624 (2023): 57–63, <https://doi.org/10.1038/s41586-023-06736-8>.
29. F. Wang, R. E. Christiansen, Y. Yu, J. Mørk, and O. Sigmund, "Maximizing the Quality Factor to Mode Volume Ratio for Ultra-small Photonic Crystal Cavities," *Applied Physics Letters* 113 (2018): 241101, <https://doi.org/10.1063/1.5064468>.
30. H. Choi, M. Heuck, and D. Englund, "Self-similar Nanocavity Design With Ultrasmall Mode Volume for Single-photon Nonlinearities," *Physical Review Letters* 118 (2017): 223605.
31. S. Hu and S. M. Weiss, "Design of Photonic Crystal Cavities for Extreme Light Concentration," *ACS Photonics* 3 (2016): 1647–1653, <https://doi.org/10.1021/acsp Photonics.6b00219>.
32. A. Gondarenko and M. Lipson, "Low Modal Volume Dipole-Like Dielectric Slab Resonator," *Optics Express* 16 (2008): 17689–17694, <https://doi.org/10.1364/OE.16.017689>.
33. M. Albrechtsen, B. Vosoughi Lahijani, and R. E. Christiansen, "Nanometer-scale Photon Confinement in Topology-optimized Dielectric Cavities," *Nature Communications* 13 (2022): 6281, <https://doi.org/10.1038/s41467-022-33874-w>.
34. M. Saldutti, M. Xiong, E. Dimopoulos, Y. Yu, M. Gioannini, and J. Mørk, "Modal Properties of Photonic Crystal Cavities and Applications to Lasers," *Nanomaterials* 11 (2021): 3030, <https://doi.org/10.3390/nano1113030>.
35. Q. Xu, B. Schmidt, S. Pradhan, and M. Lipson, "Micrometre-Scale Silicon Electro-Optic Modulator," *Nature* 435 (2005): 325–327, <https://doi.org/10.1038/nature03569>.
36. M. Eppenberger, A. Messner, and B. I. Bitachon, "Resonant Plasmonic Micro-Racetrack Modulators with High Bandwidth and High Temperature Tolerance," *Nature Photonics* 17 (2023): 360–367, <https://doi.org/10.1038/s41566-023-01161-9>.
37. M. Li, J. Ling, Y. He, U. A. Javid, S. Xue, and Q. Lin, "Lithium Niobate Photonic-Crystal Electro-Optic Modulator," *Nature Communications* 11 (2020): 4123, <https://doi.org/10.1038/s41467-020-17950-7>.
38. R. E. Christiansen and O. Sigmund, "Inverse Design in Photonics by Topology Optimization: Tutorial," *Journal of the Optical Society of America B* 38 (2021): 496, <https://doi.org/10.1364/JOSAB.406408>.
39. R. E. Christiansen, "Inverse Design of Optical Mode Converters by Topology Optimization: Tutorial," *Journal of Optics* 25 (2023): 083501, <https://doi.org/10.1088/2040-8986/acdbdd>.
40. M. Xiong, R. E. Christiansen, and F. Schröder, "Experimental Realization of Deep Sub-Wavelength Confinement of Light in a Topology-Optimized InP Nanocavity," *Optical Materials Express* 14 (2024): 397–406, <https://doi.org/10.1364/OME.513625>.
41. S. Hu, M. Khater, and R. Salas-Montiel, "Experimental Realization of Deep-subwavelength Confinement in Dielectric Optical Resonators," *Science Advances* 4 (2018): aat2355, <https://doi.org/10.1126/sciadv.aat2355>.
42. G. Işıklar, P. T. Kristensen, J. Mørk, O. Sigmund, and R. E. Christiansen, "On the Trade-off Between Mode Volume and Quality Factor in Dielectric Nanocavities Optimized for Purcell Enhancement," *Optics Express* 30 (2022): 47304–47314.
43. P. B. Deotare, M. W. McCutcheon, I. W. Frank, M. Khan, and M. Lončar, "High Quality Factor Photonic Crystal Nanobeam Cavities," *Applied Physics Letters* 94 (2009): 121106, <https://doi.org/10.1063/1.3107263>.
44. A. Mecozzi and J. Mørk, "Theory of Heterodyne Pump-Probe Experiments with Femtosecond Pulses," *Journal of the Optical Society of America B* 13 (1996): 2437–2452, <https://doi.org/10.1364/JOSAB.13.002437>.
45. P. Lunnemann, Y. Yu, K. Joanesarson, and J. Mørk, "Ultrafast Parametric Process in a Photonic-Crystal Nanocavity Switch," *Physical Review A* 99 (2019): 053835, <https://doi.org/10.1103/PhysRevA.99.053835>.
46. P. Colman, P. Lunnemann, Y. Yu, and J. Mørk, "Ultrafast Coherent Dynamics of a Photonic Crystal All-Optical Switch," *Physical Review Letters* 117 (2016): 233901, <https://doi.org/10.1103/PhysRevLett.117.233901>.
47. T. J. Johnson, M. Borselli, and O. Painter, "Self-Induced Optical Modulation of the Transmission Through a High-Q Silicon Microdisk Resonator," *Optics Express* 14 (2006): 817–831, <https://doi.org/10.1364/OPEX.14.000817>.
48. P. E. Barclay, K. Srinivasan, and O. Painter, "Nonlinear Response of Silicon Photonic Crystal Micresonators Excited via an Integrated Waveguide and Fiber Taper," *Optics Express* 13 (2005): 801–820, <https://doi.org/10.1364/OPEX.13.000801>.
49. G. Moille, S. Combré, and A. De Rossi, "Modeling of the Carrier Dynamics in Nonlinear Semiconductor Nanoscale Resonators," *Physical Review A* 94 (2016), <https://doi.org/10.1103/PhysRevA.94.023814>.
50. M. Saldutti, Y. Yu, G. Kountouris, P. T. Kristensen, and J. Mørk, "Carrier Diffusion in Semiconductor Nanoscale Resonators," *Physical Review B* 109 (2024): 245301, <https://doi.org/10.1103/PhysRevB.109.245301>.
51. C. J. Chen, J. Zheng, and T. Gu, "Selective Tuning of High-Q Silicon Photonic Crystal Nanocavities via Laser-Assisted Local Oxidation," *Optics Express* 19 (2011): 12480–12489, <https://doi.org/10.1364/OE.19.012480>.
52. H. S. Lee, S. Kiravittaya, and S. Kumar, "Local Tuning of Photonic Crystal Nanocavity Modes by Laser-Assisted Oxidation," *Applied Physics Letters* 95 (2009): 191109, <https://doi.org/10.1063/1.3262961>.

Supporting Information

Additional supporting information can be found online in the Supporting Information section.

Supporting File: lpor70582-sup-0001-SuppMat.docx